

# Gaussian Swaying : Surface-Based Framework for Aerodynamic Simulation with 3D Gaussians

Hongru Yan<sup>1,\*</sup> Xiang Zhang<sup>2</sup> Zeyuan Chen<sup>2</sup> Fangyin Wei<sup>3</sup> Zhuowen Tu<sup>2</sup>  
<sup>1</sup>Tsinghua University <sup>2</sup>UC San Diego <sup>3</sup>Princeton University

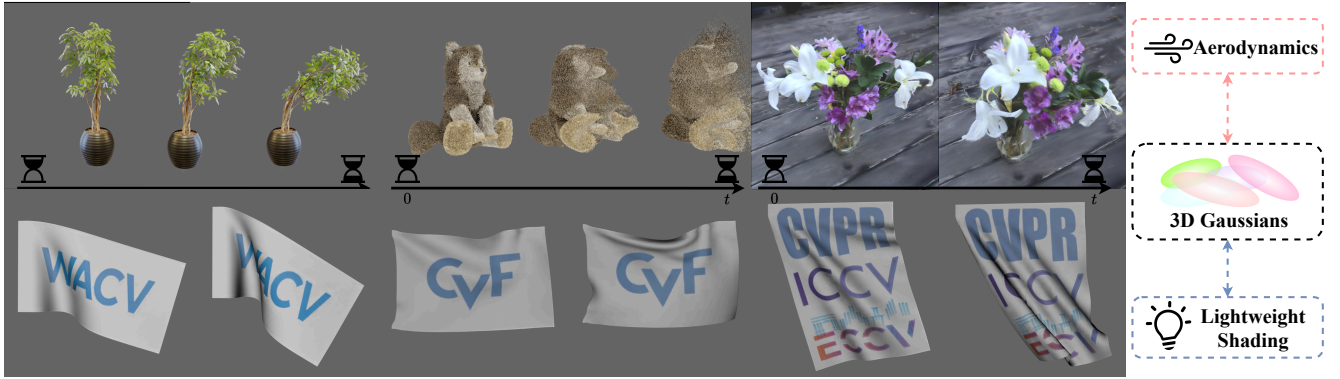


Figure 1. Gaussian Swaying is a unified surface-based framework that couples aerodynamic simulation with lightweight shading for efficient and realistic dynamics.

## Abstract

*Branches swaying in the breeze, flags rippling in the wind, and boats rocking on the water all show how aerodynamics shape natural motion – an effect crucial for realism in vision and graphics. In this paper, we present Gaussian Swaying, a surface-based framework for aerodynamic simulation using 3D Gaussians. Unlike mesh-based methods that require costly meshing, or particle-based approaches that rely on discrete positional data, Gaussian Swaying models surfaces continuously with 3D Gaussians, enabling efficient and fine-grained aerodynamic interaction. Our framework unifies simulation and rendering on the same representation: Gaussian patches, which support force computation for dynamics while simultaneously providing normals for lightweight shading. Comprehensive experiments on both synthetic and real-world datasets across multiple metrics demonstrate that Gaussian Swaying achieves state-of-the-art performance and efficiency, offering a scalable approach for realistic aerodynamic scene simulation.*

\*Work done during internship at UC San Diego.

## 1. Introduction

Wind-driven motion is a defining aspect of our daily visual experience: branches sway, flags billow, and boats rock on the water. Capturing such dynamics is essential for realism in computer vision and graphics [43]. Traditional simulation techniques such as the Material Point Method (MPM) [20, 50] or Position-Based Dynamics (PBD) [33, 36] are versatile across materials, but they incur high computational costs and struggle to meet the demand for fast yet visually faithful simulation. Moreover, because wind interactions are fundamentally surface-driven, these methods typically require explicit mesh reconstruction [11, 23], which complicates simulation for complex or evolving structures.

Recent advances in neural scene representations, such as NeRF [34] and Gaussian Splatting [25], have opened new possibilities for efficient dynamic simulation [15, 27, 54, 57, 60, 67]. For instance, PhysGaussian [54] integrates Gaussian kernels with MPM particles to accelerate simulation and rendering. However, such approaches remain particle-based, modeling dynamics as collections of discrete points [42]. While efficient, they lack explicit surface awareness, limiting their ability to capture fine-grained

aerodynamic interactions, where surface normals and areas directly govern how forces are applied.

In this work, we introduce Gaussian Swaying, a surface-based framework for aerodynamic simulation with 3D Gaussians. Unlike particle-only or mesh-based approaches, Gaussian Swaying treats Gaussian kernels as continuous surface patches characterized by normals and areas, enabling direct aerodynamic force computation. The same representation supports lightweight shading tied to surface properties, producing a realistic appearance that adapts naturally to lighting and view direction. By unifying simulation and rendering on a single surface-based representation, Gaussian Swaying eliminates costly intermediate meshing steps, improving both efficiency and fidelity.

We validate Gaussian Swaying through extensive experiments on synthetic and real-world datasets, including a custom flag simulation benchmark. Results show that Gaussian Swaying achieves state-of-the-art performance and efficiency for aerodynamics, providing a practical and scalable solution for realistic aerodynamic simulation in vision and graphics.

Our key contributions are summarized as follows:

- **Surface-based aerodynamic framework.** We propose Gaussian Swaying, a novel framework for simulating aerodynamics with 3D Gaussians, eliminating costly meshing while supporting efficient, visually realistic simulation.
- **Surface-aware simulation and rendering.** We formulate Gaussians as continuous surface patches, rather than discrete particles, to unify aerodynamic force computation with lightweight shading for realism.
- **Extensive evaluation.** We conduct comprehensive experiments on both synthetic and real-world datasets, including a new flag simulation benchmark, demonstrating state-of-the-art accuracy and efficiency.

## 2. Related Work

### 2.1. Neural Scene Representations

Neural scene representations have advanced rapidly for geometry modeling and downstream vision tasks. Some approaches focus on explicit 3D representations such as point clouds [55, 59], voxels [9], and meshes [48, 53, 64]. In contrast, implicit representations define continuous functions over space: Signed Distance Fields (SDFs) [30, 63, 65] model geometry via a continuous distance function, while Neural Radiance Fields (NeRF) [34] extend implicit modeling to volumetric radiance, enabling high-quality novel-view synthesis. However, NeRF relies on fully connected networks and massive ray queries, resulting in slow training and inference. Subsequent works have improved its efficiency [16, 37] and extended its capabilities to high-fidelity synthesis [56], multi-view generalization [5, 31, 66], and

scene understanding [6, 29, 35].

More recently, 3D Gaussian Splatting [25] has emerged as an efficient alternative, directly representing scenes with explicit Gaussian primitives for real-time rendering. This representation has been applied to surface reconstruction [7, 17, 24], object detection [58], semantic understanding [47], and editing [8, 51]. Notably, works such as Gaussian-Shader [24], SuGaR [17], and Gaussian-Det [58] highlight the strength of Gaussians in capturing surface-level details. These advances motivate our use of 3D Gaussians as surface representations, extending them beyond static reconstruction or recognition toward dynamic aerodynamic simulation.

### 2.2. Dynamic Scenes and Simulations

Modeling dynamic scenes with neural representations such as NeRF and 3D Gaussians has become an active area in computer vision [4, 28, 46]. Several works extend NeRF by incorporating time as an additional parameter to capture non-rigid motion [38, 39], while others achieve efficient dynamic view synthesis with Gaussian-based representations [12]. Beyond view synthesis, researchers have also explored simulation. NeRF-Editing [60] and Deforming-NeRF [57] extract meshes or deformation cages from NeRFs, while PAC-NeRF [27] integrates the material point method (MPM) with particles, and PIE-NeRF [15] introduces mesh-less least squares kernels. PhysGaussian [54] represents a milestone by connecting Gaussian kernels with MPM particles for realistic and efficient physics simulation, followed by Spring-Gaus [67], which employs a spring-mass model for system identification.

However, existing Gaussian-based simulation methods treat Gaussian kernels purely as positional primitives for physics engines, without explicitly modeling surfaces. This limits their ability to capture fine-grained aerodynamic interactions that are inherently surface-driven. Our work addresses this gap by formulating Gaussians as continuous surface patches and incorporating them directly into the simulation process, enabling smoother and more realistic surface dynamics.

### 2.3. Aerodynamic Simulation

Aerodynamic simulation has traditionally relied on physics-based methods such as the finite element method (FEM), the material point method (MPM) [20, 22, 50], and position-based dynamics (PBD) [33, 36]. While these approaches are versatile across different physical settings, achieving real-time wind-driven dynamics with high visual fidelity remains a long-standing challenge in computer vision and graphics [18, 23, 32, 49]. Moreover, such methods typically require extensive manual preparation, including mesh construction and vertex constraint tuning, which makes them less suitable for automatic or complex dynamic scenes. In-

corporating realistic shading effects [2, 10] further increases computational cost, limiting their practicality for efficient simulation–rendering pipelines.

Motivated by these limitations, we propose a surface-based yet mesh-free framework that directly leverages 3D Gaussians as continuous surface representations. Our method eliminates costly meshing, reduces manual setup, and integrates lightweight shading, enabling efficient aerodynamic simulation with compelling visual realism.

### 3. Method

We present Gaussian Swaying, a unified surface-based framework for aerodynamics, with an overview illustrated in Fig. 2. Our approach formulates 3D Gaussians as surface patches, enabling aerodynamic simulation and realistic rendering within the same representation. In this section, we first review the relevant preliminaries, then describe the proposed formulation in detail, including surface-aware Gaussian modeling, aerodynamic simulation, and lightweight shading.

#### 3.1. Preliminaries

**Continuum Mechanics.** Continuum mechanics describes the motion of a deformable body via a deformation map  $\mathbf{x} = \phi(\mathbf{X}, t)$  from material space  $\Omega^0$  to world space  $\Omega^t$  at time  $t$ . The deformation gradient  $\mathbf{F} = \frac{\partial \phi}{\partial \mathbf{X}}(\mathbf{X}, t)$  characterizes local rotation, stretch, and shear [3].  $\mathbf{F}$  is updated via conservation of mass and momentum, which is given by:

$$\frac{D\rho}{Dt} + \rho \nabla \cdot \mathbf{v} = 0 \quad (1)$$

$$\rho \frac{D\mathbf{v}}{Dt} = \nabla \cdot \boldsymbol{\sigma} + \mathbf{f}^{\text{ext}} \quad (2)$$

where  $\mathbf{f}^{\text{ext}}$  is the external force and  $\boldsymbol{\sigma}$  is the Cauchy stress.

**Material Point Method.** The material point method solves the above conservation laws by combining Eulerian grids with Lagrangian particles [22, 49]. It is widely used for simulating diverse materials [21, 26, 41, 61]. MPM alternates between two stages: (i) Particle-to-Grid (P2G), where momentum and mass are transferred from particles to the grid, and (ii) Grid-to-Particle (G2P), where updated velocities are mapped back:

$$\frac{m_i}{\Delta t} (\mathbf{v}_i^{n+1} - \mathbf{v}_i^n) = - \sum_p \tau_p^n \nabla w_{ip}^n V_p^0 + \mathbf{f}_i^{\text{ext}} \quad (3)$$

where  $i$  and  $p$  denote grid nodes and particles, respectively.  $\tau_p = \det(\mathbf{F}_p) \sigma_p$  is the Kirchhoff stress,  $V_p^0$  is the initial particle volume, and  $w_{ip}^n$  is the B-spline kernel evaluated at particle position  $\mathbf{x}_p^n$ . Further algorithmic details can be found in supplementary materials.

**Gaussian Splatting.** 3D Gaussian Splatting [25] represents a scene using Gaussian primitives for real-time rendering. Each Gaussian  $\mathbf{G}_p = \{\mathbf{x}_p, \mathbf{A}_p, \sigma_p, \mathbf{C}_p\}$  is parameterized by position  $\mathbf{x}_p$ , covariance matrix  $\mathbf{A}_p$ , opacity  $\sigma_p$ , and spherical harmonic (SH) coefficients  $\mathbf{C}_p$ . The Gaussian color  $\mathbf{c}_p$  is derived from  $\mathbf{C}_p$  and the view direction, and the final pixel color is obtained through  $\alpha$ -blending:

$$C = \sum_{i=1}^n \mathbf{c}_i \alpha_i \prod_{j=1}^{i-1} (1 - \alpha_j) \quad (4)$$

where  $n$  is the number of Gaussians. Parameters of Gaussians are optimized via back-propagation during training.

#### 3.2. Gaussian Swaying

##### 3.2.1. Surface Formulation

Unlike PhysGaussian [54] and other point-based methods that treat Gaussians as volumetric particles, Gaussian Swaying adopts a surface-based representation. Point-based formulations are effective for general dynamics but lack explicit surface awareness, which is essential for aerodynamic interactions.

We define a Gaussian surface patch as:

$$\mathbf{G}_p^{\text{surf}} = \{\mathbf{x}_p, \mathcal{A}_p, \mathbf{N}_p, \sigma_p, \mathbf{c}_p\} \quad (5)$$

where  $\mathbf{x}_p$  is the position,  $\sigma_p$  the opacity, and  $\mathbf{c}_p$  the rendering color (see Sec. 3.2.4). The new surface-specific attributes are the patch area  $\mathcal{A}_p$  and surface normal  $\mathbf{N}_p$ .

The surface area is derived from the Gaussian scaling  $\mathbf{S}_p = \{\mathbf{S}_p^1, \mathbf{S}_p^2, \mathbf{S}_p^3\}$ , ordered from largest to smallest:

$$\mathcal{A}_p = \pi \frac{\mathbf{S}_p^1 \cdot \mathbf{S}_p^2 \cdot \mathbf{S}_p^3}{\min(\mathbf{S}_p^1, \mathbf{S}_p^2, \mathbf{S}_p^3)} = \pi \mathbf{S}_p^1 \mathbf{S}_p^2 \quad (6)$$

The initial surface normal  $\mathbf{N}_p$  is defined along the smallest axis [17].

During simulation, a Gaussian patch evolves in world space under local deformation. Its center and covariance update according to the deformation map  $\phi(\mathbf{X}_p, t)$  and gradient  $\mathbf{F}_p(t)$ :

$$\mathbf{x}_p(t) = \phi(\mathbf{X}_p, t), \quad \mathbf{a}_p(t) = \mathbf{F}_p(t) \mathbf{A}_p \mathbf{F}_p(t)^T \quad (7)$$

assuming local affine transformations as in [54]. The surface normal is updated as:

$$\mathbf{n}_p(t) = \frac{\mathbf{F}_p(t)^{-T} \mathbf{N}_p}{\|\mathbf{F}_p(t)^{-T} \mathbf{N}_p\|} \quad (8)$$

As illustrated in Fig. 3, Gaussian patches approximate object surfaces without requiring meshing. Each patch provides area and normal information while being coupled with the MPM grid, forming an efficient bridge between surface geometry and physical dynamics. This surface-based formulation enables accurate aerodynamic force modeling and efficient shading within a unified framework.

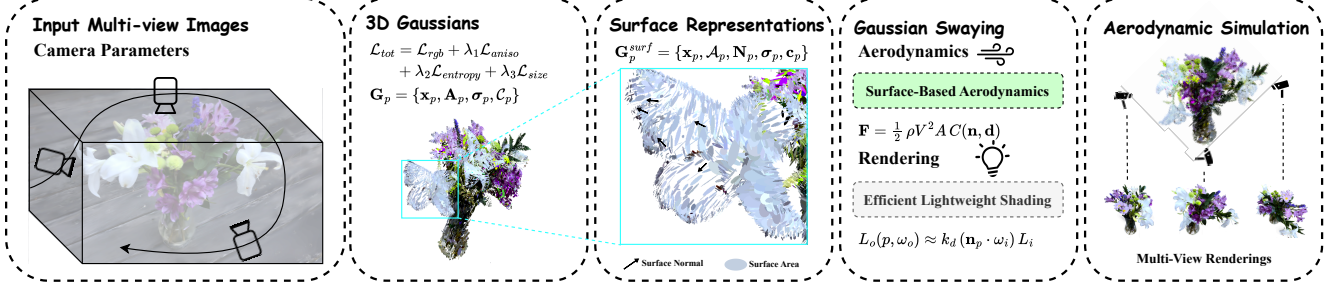


Figure 2. **Pipeline Overview.** Gaussian Swaying is a unified surface-based framework for aerodynamics. By representing 3D Gaussians as continuous surface patches, it integrates aerodynamic simulation and realistic rendering within the same representation. Gaussian patches support aerodynamic force computation while also providing normals for lightweight shading, enabling realistic and efficient visual effects. Multi-view renderings of simulation results are shown on the right.

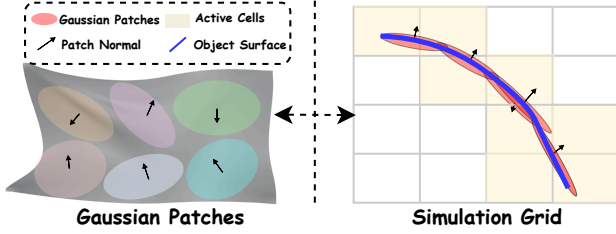


Figure 3. **Surface Formulation.** Gaussian Swaying represents objects as Gaussian surface patches, each defined by a normal and effective area, enabling efficient surface-specific interactions. Left: a deforming flag modeled as Gaussian patches. Right: coupling with the MPM grid, where patches provide surface attributes and receive deformation updates. Blue line indicates the ground-truth surface, and shaded cells mark active simulation regions.

### 3.2.2. Training

During training, we encourage Gaussians to stay close to object surfaces and maintain surface fidelity under deformation. To this end, we adopt the anisotropy loss [14, 54] and entropy loss [12]:

$$\mathcal{L}_{\text{aniso}} = \frac{1}{n} \sum_{i=1}^n \max \left\{ \frac{S_i^1}{S_i^2} - a, 0 \right\} \quad (9)$$

$$\mathcal{L}_{\text{entropy}} = -\frac{1}{n} \sum_{i=1}^n \sigma_i \log \sigma_i \quad (10)$$

with  $a = 1.1$ . The anisotropy loss prevents Gaussians from becoming overly elongated, while the entropy loss drives opacities toward 0 or 1, pushing Gaussians to align with surfaces.

We further introduce a size loss to constrain Gaussian scale within surface ranges:

$$\mathcal{L}_{\text{size}} = \frac{1}{n} \sum_{i=1}^n \max \{ S_i^1 - b, 0 \} \quad (11)$$

where  $b = 0.008$ . The final training objective is:

$$\mathcal{L}_{\text{tot}} = \mathcal{L}_{\text{rgb}} + \lambda_1 \mathcal{L}_{\text{aniso}} + \lambda_2 \mathcal{L}_{\text{entropy}} + \lambda_3 \mathcal{L}_{\text{size}} \quad (12)$$

where  $\mathcal{L}_{\text{rgb}}$  is the standard RGB reconstruction loss from [25]. We set  $\lambda_1 = 10$ ,  $\lambda_2 = \lambda_3 = 0.01$ . Further implementation details are provided in the supplementary material.

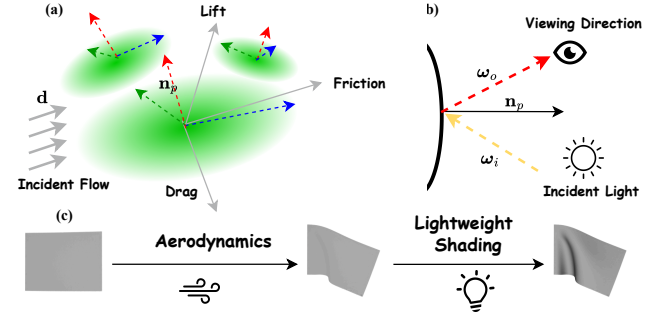


Figure 4. **Illustration of Aerodynamics and Lightweight Shading.** (a) Incident flow (gray) and resulting aerodynamic forces on a Gaussian patch, with coordinate axes shown in red, green, and blue. (b) Principle of lightweight shading: the full BSDF formulation is approximated by an efficient local shading model. (c) Flag simulation results: (1) aerodynamics only, and (2) aerodynamics with lightweight shading.

### 3.2.3. Aerodynamics

Aerodynamic forces arise from surface pressure and shear stress distributions governed by the Navier-Stokes equations [1]:

$$\mathbf{F} = \int_A (-p\mathbf{n} + \boldsymbol{\tau} \cdot \mathbf{n}) dA \quad (13)$$

where  $p$  is pressure,  $\boldsymbol{\tau}$  is viscous stress, and  $\mathbf{n}$  is the surface normal.

In practice, this formulation is commonly approximated by the classical dynamic pressure model through non-



dimensionalization:

$$\mathbf{F} = \frac{1}{2} \rho V^2 A C(\mathbf{n}, \mathbf{d}) \quad (14)$$

where  $\rho$  is fluid density,  $V$  the relative velocity,  $A$  the effective surface area, and  $C$  a non-dimensional coefficient depending on the surface normal  $\mathbf{n}$  and flow direction  $\mathbf{d}$ .

For a Gaussian surface patch  $p$ , the aerodynamic force is modeled as the combination of drag, friction, and lift:

$$\mathbf{f}_p = \frac{1}{2} \rho v_{r,p}^2 A_p (C_D \mathbf{n}_p + C_F \hat{\mathbf{d}}^t + C_L (\mathbf{d} \times \mathbf{n}_p)) \quad (15)$$

where subscript  $p$  indicates patch-specific quantities.  $\hat{\mathbf{d}}^t$  is the tangential projection of the flow direction  $\mathbf{d}$  onto the local surface tangent plane. The aerodynamic coefficients  $C_D, C_F, C_L$  represent the drag, friction, and lift responses of each surface patch under incident flow. We follow standard practice in computational fluid dynamics. In implementation, we fix them for representative values obtained from established empirical tables (please refer to supplementary materials). An illustration is provided in Fig. 4 (a).

The characteristic swaying effect arises from fluctuations in flow strength and direction. To capture this behavior and improve visual realism, we perturb the incident velocity during simulation as

$$v' = v(1 + \epsilon), \quad \epsilon \sim \mathcal{U}(-\delta, \delta) \quad (16)$$

where  $\delta$  controls the perturbation strength and  $\mathcal{U}(-\delta, \delta)$  is a uniform distribution.

### 3.2.4. Lightweight Shading

The outgoing radiance at a surface point  $p$  in direction  $\omega_o$  is defined by the rendering equation with the bidirectional scattering distribution function (BSDF):

$$L_o(p, \omega_o) = \int_{\Omega} f_{\text{BSDF}}(p, \omega_i, \omega_o) L_i(p, \omega_i) (\mathbf{n}_p \cdot \omega_i) d\omega_i \quad (17)$$

where  $f_{\text{BSDF}}$  describes material response and  $L_i$  is incident radiance from direction  $\omega_i$ .

To achieve real-time efficiency, graphics systems often approximate the BSDF with local illumination models such as the Phong model, consisting of ambient, diffuse, and specular components:

$$L_o(p, \omega_o) = k_a L_a + k_d (\mathbf{n}_p \cdot \omega_i) L_i + k_s (\mathbf{r} \cdot \omega_o)^\alpha \quad (18)$$

where  $k_a, k_d, k_s$  are ambient, diffuse, and specular coefficients,  $\alpha$  is the shininess exponent, and  $\mathbf{r}$  is the reflection vector:

$$\mathbf{r} = 2(\mathbf{n}_p \cdot \omega_i) \mathbf{n}_p - \omega_i \quad (19)$$

Details are visualized in Fig. 4 (b). For typical cloth-like objects such as flags, specular effects are minimal. In

these cases, we approximate shading with a diffuse formulation directly tied to Gaussian surface properties. Specifically, given a unit light vector  $\mathbf{L}$ , the diffuse shading term at timestamp  $t$  is then:

$$s_p(t) = \max(0, \mathbf{n}_p(t) \cdot \mathbf{L}) \quad (20)$$

The rendered color for a Gaussian patch  $p$  is computed as

$$\mathbf{c}_p(t) = \mathbf{c}_{p,0}(t) s_p(t) \quad (21)$$

where albedo and light intensity are absorbed into the intrinsic color  $\mathbf{c}_{p,0}(t)$ , which is obtained from the spherical harmonic coefficients  $\mathcal{C}_p$ .

This formulation yields smooth shading transitions across surfaces without requiring mesh reconstruction or UV unwrapping. As illustrated in Fig. 4 (c), shading becomes a natural extension of surface-based Gaussian tracking, enabling visually compelling yet lightweight rendering.

## 4. Experiments

We evaluate Gaussian Swaying on synthetic and real-world datasets to assess its effectiveness, efficiency, and visual quality in simulating wind-driven dynamics. Comparative studies demonstrate advantages over state-of-the-art baselines, and ablation studies further validate the design choices.

### 4.1. Evaluation of Aerodynamics

**Datasets.** We test Gaussian Swaying across diverse aerodynamic scenarios. Synthetic datasets include *Ficus* and *Sand*, generated by BlenderNeRF [40]. Real-world scenes include *Vase* from the NeRF dataset [34], and *Telephone* and *Alocasia* from PhysDremer [62]. For real-world scenes, initial point clouds and camera parameters are reconstructed using COLMAP [44, 45].

**Implementation Details.** Gaussian Swaying is implemented on top of the MPM engine from [54, 68]. Simulation regions, object materials, and parameters are manually specified, and Gaussian kernels with opacity below a threshold are filtered out. Wind speed, aerodynamic coefficients, and noise settings are detailed in the supplementary. All experiments, including Gaussian training and simulation, are performed on a single NVIDIA RTX 4090 GPU.

**Results.** Qualitative results are shown in Fig. 5, with additional videos provided in the supplementary material. In *Ficus* and *Leaves*, Gaussian Swaying captures realistic swaying and bending of branches, faithfully modeling surface-level wind interactions. In real-world cases such as *Vase* and *Alocasia*, our method produces visually convincing motion

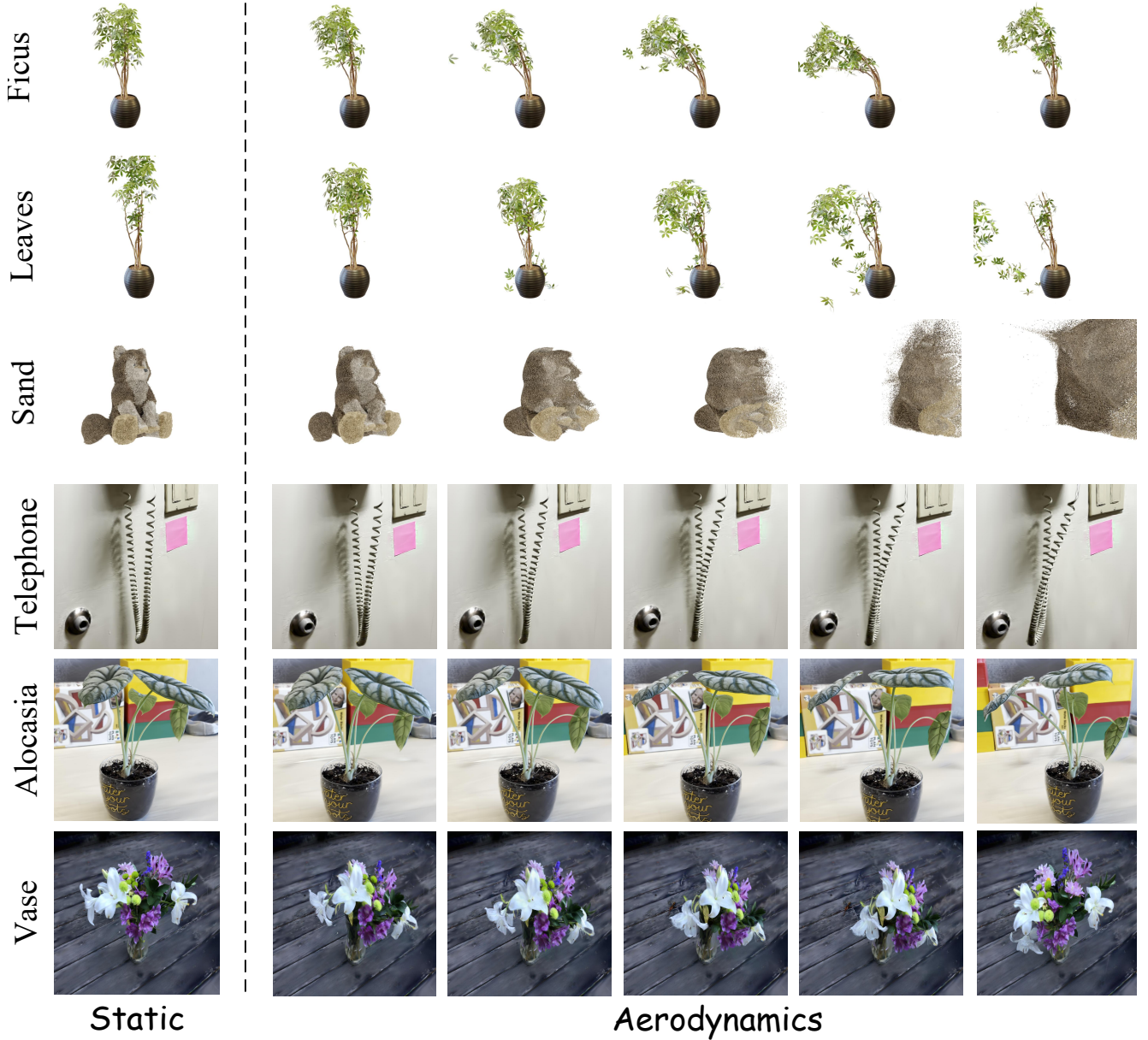


Figure 5. **Qualitative Results of Aerodynamics.** Gaussian Swaying generates realistic physics-based motion using 3D Gaussians across diverse materials.

while preserving surface fidelity. Comparative qualitative results against baselines are included in the supplementary.

## 4.2. Flag Simulation

**Settings and Dataset.** To evaluate the ability of Gaussian Swaying to handle complex and flexible surfaces, we curate a custom **Flag Simulation Dataset** with BlenderNeRF [40]. We use 200 images for scene reconstruction and reserve one unseen view for evaluation, aligned collinearly with the ini-

tial normals to satisfy Eq. (20). Three distinct motion patterns are generated, with simulation parameters (*e.g.*, material density, flow intensity, *etc.*) matched between Gaussian Swaying and BlenderNeRF.

**Pattern-1:** Flag pinned on the left edge and driven only by gravity. The flag is pure white to highlight shading effects.

**Pattern-2:** Flag anchored at three corners, with the bottom-left corner free. Motion is driven by gravity and incident flow to the right.

Table 1. **Quantitative Comparison on Flag Simulation.** Metrics include PSNR, Chamfer Distance (CD), and Fréchet Video Distance (FVD), computed against reference videos. Each pattern is evaluated over 250-frame sequences. Best results are highlighted in bold.

Method	Pattern-1			Pattern-2			Pattern-3		
	PSNR $\uparrow$	CD $\downarrow$	FVD $\downarrow$	PSNR $\uparrow$	CD $\downarrow$	FVD $\downarrow$	PSNR $\uparrow$	CD $\downarrow$	FVD $\downarrow$
NeRF-Editing [60]	14.53	0.0540	413.39	15.94	0.0197	569.68	17.57	0.0228	382.69
Deforming-NeRF [57]	15.53	0.0466	330.15	19.41	0.0245	430.01	17.33	0.0251	359.05
PAC-NeRF [27]	15.78	0.0526	275.85	20.95	0.0210	437.91	18.19	0.0212	437.71
PIE-NeRF [15]	17.73	0.0269	152.79	19.29	0.0111	383.25	14.13	0.0308	529.19
Spring-Gaus [67]	19.20	0.0288	140.01	21.31	0.0086	359.86	14.92	0.0196	556.86
PhysGaussian [54]	19.75	0.0215	158.16	21.96	0.0054	327.68	14.44	0.0263	628.58
Gaussian Swaying (ours)	<b>21.44</b>	<b>0.0178</b>	<b>50.47</b>	<b>22.26</b>	<b>0.0052</b>	<b>290.21</b>	<b>18.60</b>	<b>0.0066</b>	<b>219.94</b>

**Pattern-3:** Large flag suspended from the top, driven by gravity and rightward flow.

Lightweight shading is enabled for all patterns, under a single area light oriented perpendicular to the flag plane. For evaluation, all baselines use identical material parameters and flow strength. The background is set to black to remove external influences.

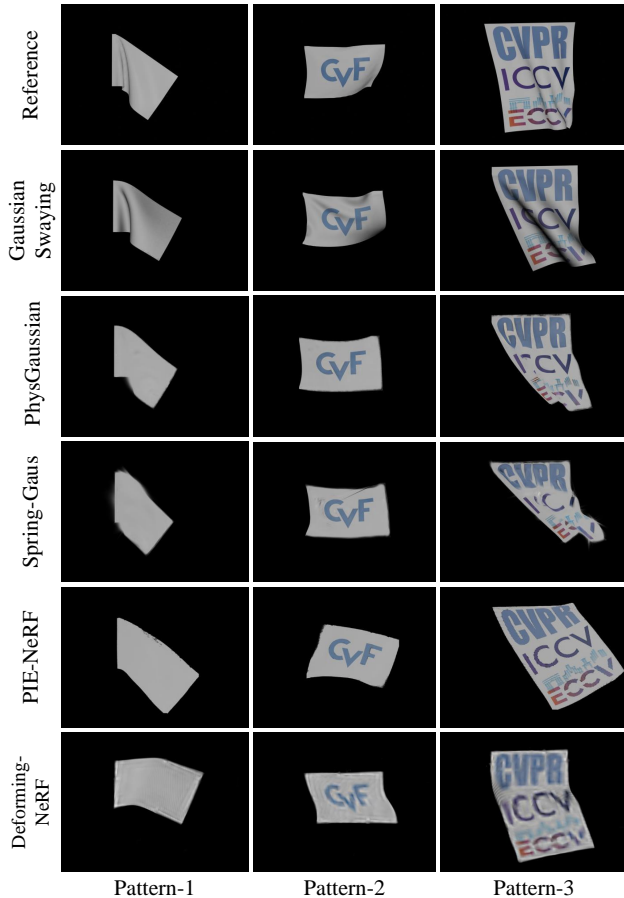


Figure 6. **Qualitative Comparisons on Flag Simulation Dataset.** The results are displayed on testing views.

**Quantitative and Qualitative Comparisons.** We compare Gaussian Swaying against state-of-the-art frameworks for dynamic deformation with neural scene representations. NeRF-based baselines include NeRF-Editing [60], Deforming-NeRF [57], PAC-NeRF [27], and PIE-NeRF [15]. Gaussian-based baselines include PhysGaussian [54] and Spring-Gaus [67].

Evaluation metrics are Peak Signal-to-Noise Ratio (PSNR) [19], Chamfer Distance (CD) [13], and Fréchet Video Distance (FVD) [52], computed using official implementations of the baselines. Each pattern is simulated for 250 frames at  $1920 \times 1080$  resolution.

As shown in Tab. 1, Gaussian Swaying achieves state-of-the-art performance across all metrics, with significant improvements in both reconstruction fidelity and temporal coherence. Qualitative results in Fig. 6 further highlight the advantages: Gaussian Swaying produces smooth shading transitions and realistic surface ripples consistent with reference videos. In contrast, particle-based methods (PIE-NeRF, PhysGaussian, PAC-NeRF, Spring-Gaus) struggle to capture surface-specific dynamics, while mesh-based methods (Deforming-NeRF, NeRF-Editing) require manual vertex manipulation and suffer from coarse reconstructions and surface discrepancies.

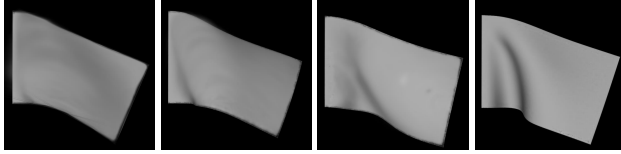
#### 4.3. Ablation Studies and Analysis

We conduct ablations to validate the design of Gaussian Swaying and analyze its efficiency.

**Training Losses.** We first study the impact of the proposed training losses. As shown in Fig. 7, the baseline (I) produces blurred surfaces. Adding anisotropy and entropy losses (II, III) improves sharpness but leaves artifacts. Incorporating size loss (IV) yields clear surface ripples and the most realistic results. We also provide ablation studies on choices of hyperparameters in supplementary materials.

**Design Components.** We ablate the key components of Gaussian Swaying, with results summarized in Tab. 2 and visualized in Fig. 8.

- **No Flow Randomization.** Disabling randomness in flow



I. Vanilla GS II. I+Anisotropy Loss III. II+Entropy Loss IV. III+Size Loss

Figure 7. **Ablation on Training Losses for 3D Gaussians.** Anisotropy and entropy losses improve rendering quality over vanilla Gaussian Splatting but still yield blurred regions. Adding size loss resolves this issue, producing realistic surface ripples.

intensity leads to unnatural motion (FVD +114%).

- **No Lightweight Shading.** Removing shading has little impact on dynamics (+0.11%), but eliminates surface ripples (see Fig. 8), reducing visual realism.
- **No Surface Modeling.** Applying aerodynamic forces directly on Gaussians without surface formulation causes severe degradation (FVD +335%, CD +329%, PSNR −20.4%), performing even worse than PhysGaussian.

Table 2. **Quantitative Ablation on Design Choices in Gaussian Swaying.** Comparison with PhysGaussian using PSNR, Chamfer Distance (CD), and Fréchet Video Distance (FVD).

Description	PSNR $\uparrow$	CD $\downarrow$	FVD $\downarrow$
PhysGaussian	14.44	0.0263	646.51
Gaussian Swaying (ours)	<b>18.60</b>	<b>0.0066</b>	<b>219.94</b>
Do Not Randomize Flow Intensity	17.93	0.0070	468.72
Disable Lightweight Shading	18.38	0.0069	243.57
W/o Surface Modeling in Aerodynamics	14.80	0.0277	954.36

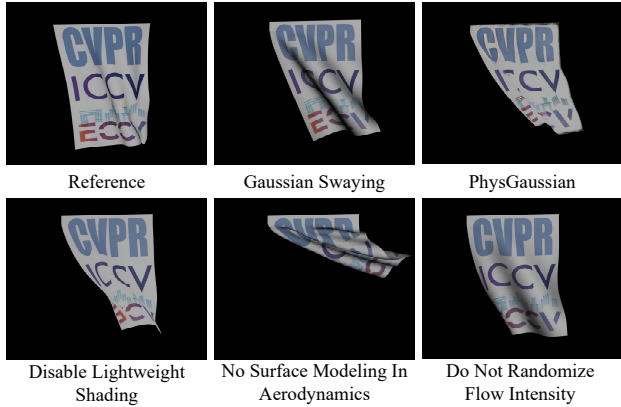


Figure 8. **Qualitative Comparisons and Ablation Studies.** *Top row:* comparison of Gaussian Swaying with PhysGaussian and reference video. *Bottom row:* ablation of key design choices in Gaussian Swaying, illustrated using Pattern-3.

**Solid Objects.** We also study solid objects by filling their interior with Gaussians of identical density and volume (Fig. 9). Since Gaussian Swaying applies aerodynamic forces only to surface Gaussians, internal Gaussians remain

unaffected. This confirms that surface-aware modeling is essential for aerodynamics.



Figure 9. **Simulations with different recipients of aerodynamic forces.**

**Model Efficiency.** We compare per-frame runtime (simulation + rendering) and GPU memory on the flag simulation dataset. As shown in Tab. 3, Gaussian Swaying achieves significant improvements, reducing runtime by 47.8% and memory by 35.1% compared to PIE-NeRF. Compared with PhysGaussian, Gaussian Swaying is 25% faster and uses 29.4% less memory.

Table 3. **Efficiency Comparisons.** Per-frame processing time and GPU memory usage on the flag simulation dataset.

Method	Time (s) $\downarrow$	GPU Memory (GB) $\downarrow$
Deforming-NeRF	20.01	36.3
PIE-NeRF	0.23	7.4
PhysGaussian	0.16	6.8
<b>Gaussian Swaying (Ours)</b>	<b>0.12</b>	<b>4.8</b>

**Discussion.** Our proposed surface-aware modeling offers a continuous representation that avoids volumetric redundancy and gaps, reducing both storage for Gaussians and per-step simulation cost. Moreover, the unified pipeline enables the same Gaussian patches to support aerodynamic force computation and rendering, eliminating the need for separate primitives. These design choices directly contribute to the efficiency gains observed in our experiments, underscoring the practicality of Gaussian Swaying for large-scale and real-time applications.

## 5. Conclusion

We presented Gaussian Swaying, a surface-based framework for aerodynamic simulation with 3D Gaussians. By modeling Gaussian patches as surface representations, Gaussian Swaying unifies aerodynamic simulation and rendering without requiring meshing. Aerodynamic forces are computed per patch, while lightweight shading provides efficient, realistic appearance. Experiments on synthetic and real-world datasets, including a custom flag simulation benchmark, demonstrate that Gaussian Swaying achieves state-of-the-art efficiency and visual fidelity.



## Acknowledgment

This work is supported by NSF award IIS-2127544 and NSF award IIS-2433768.

## References

- [1] John Anderson. *EBOOK: Fundamentals of Aerodynamics (SI units)*. McGraw hill, 2011. 4
- [2] Jonathan T Barron and Jitendra Malik. Shape, illumination, and reflectance from shading. *IEEE transactions on pattern analysis and machine intelligence*, 37(8):1670–1687, 2014. 3
- [3] Javier Bonet and Richard D Wood. *Nonlinear continuum mechanics for finite element analysis*. Cambridge university press, 1997. 3
- [4] Piotr Borycki, Weronika Smolak, Joanna Waczyńska, Marcin Mazur, Sławomir Tadeja, and Przemysław Spurek. Gasp: Gaussian splatting for physic-based simulations. *arXiv preprint arXiv:2409.05819*, 2024. 2
- [5] Anpei Chen, Zexiang Xu, Fuqiang Zhao, Xiaoshuai Zhang, Fanbo Xiang, Jingyi Yu, and Hao Su. Mvsnr: Fast generalizable radiance field reconstruction from multi-view stereo. In *Proceedings of the IEEE/CVF international conference on computer vision*, pages 14124–14133, 2021. 2
- [6] Honghua Chen, Chen Change Loy, and Xingang Pan. Mvip-nerf: Multi-view 3d inpainting on nerf scenes via diffusion prior. In *Proceedings of the IEEE/CVF Conference on Computer Vision and Pattern Recognition*, pages 5344–5353, 2024. 2
- [7] Hanlin Chen, Fangyin Wei, Chen Li, Tianxin Huang, Yunsong Wang, and Gim Hee Lee. Vcr-gaus: View consistent depth-normal regularizer for gaussian surface reconstruction. *Advances in Neural Information Processing Systems*, 37: 139725–139750, 2024. 2
- [8] Yiwen Chen, Zilong Chen, Chi Zhang, Feng Wang, Xiaofeng Yang, Yikai Wang, Zhongang Cai, Lei Yang, Huaping Liu, and Guosheng Lin. Gaussianeditor: Swift and controllable 3d editing with gaussian splatting. In *Proceedings of the IEEE/CVF conference on computer vision and pattern recognition*, pages 21476–21485, 2024. 2
- [9] Christopher B Choy, Danfei Xu, JunYoung Gwak, Kevin Chen, and Silvio Savarese. 3d-r2n2: A unified approach for single and multi-view 3d object reconstruction. In *European conference on computer vision*, pages 628–644. Springer, 2016. 2
- [10] Robert L Cook, Thomas Porter, and Loren Carpenter. Distributed ray tracing. In *Proceedings of the 11th annual conference on Computer graphics and interactive techniques*, pages 137–145, 1984. 3
- [11] Crispin Deul, Tassilo Kugelstadt, Marcel Weiler, and Jan Bender. Direct position-based solver for stiff rods. In *Computer Graphics Forum*, pages 313–324. Wiley Online Library, 2018. 1
- [12] Yuanxing Duan, Fangyin Wei, Qiyu Dai, Yuhang He, Wenzheng Chen, and Baoquan Chen. 4d-rotor gaussian splatting: towards efficient novel view synthesis for dynamic scenes. In *ACM SIGGRAPH 2024 Conference Papers*, pages 1–11, 2024. 2, 4
- [13] Haoqiang Fan, Hao Su, and Leonidas J Guibas. A point set generation network for 3d object reconstruction from a single image. In *Proceedings of the IEEE conference on computer vision and pattern recognition*, pages 605–613, 2017. 7
- [14] Yutao Feng, Xiang Feng, Yintong Shang, Ying Jiang, Chang Yu, Zeshun Zong, Tianjia Shao, Hongzhi Wu, Kun Zhou, Chenfanfu Jiang, et al. Gaussian splashing: Dynamic fluid synthesis with gaussian splatting. *arXiv preprint arXiv:2401.15318*, 2024. 4
- [15] Yutao Feng, Yintong Shang, Xuan Li, Tianjia Shao, Chenfanfu Jiang, and Yin Yang. Pie-nerf: Physics-based interactive elastodynamics with nerf. In *Proceedings of the IEEE/CVF Conference on Computer Vision and Pattern Recognition*, pages 4450–4461, 2024. 1, 2, 7
- [16] Sara Fridovich-Keil, Alex Yu, Matthew Tancik, Qinhong Chen, Benjamin Recht, and Angjoo Kanazawa. Plenoxels: Radiance fields without neural networks. In *Proceedings of the IEEE/CVF conference on computer vision and pattern recognition*, pages 5501–5510, 2022. 2
- [17] Antoine Guédon and Vincent Lepetit. Sugar: Surface-aligned gaussian splatting for efficient 3d mesh reconstruction and high-quality mesh rendering. In *Proceedings of the IEEE/CVF Conference on Computer Vision and Pattern Recognition*, pages 5354–5363, 2024. 2, 3
- [18] Xuchen Han, Theodore F Gast, Qi Guo, Stephanie Wang, Chenfanfu Jiang, and Joseph Teran. A hybrid material point method for frictional contact with diverse materials. *Proceedings of the ACM on Computer Graphics and Interactive Techniques*, 2(2):1–24, 2019. 2
- [19] Alain Hore and Djemel Ziou. Image quality metrics: Psnr vs. ssim. In *2010 20th International Conference on Pattern Recognition*, pages 2366–2369. IEEE, 2010. 7
- [20] Yuanming Hu, Yu Fang, Ziheng Ge, Ziyin Qu, Yixin Zhu, Andre Pradhana, and Chenfanfu Jiang. A moving least squares material point method with displacement discontinuity and two-way rigid body coupling. *ACM Transactions on Graphics (TOG)*, 37(4):1–14, 2018. 1, 2
- [21] Chenfanfu Jiang, Craig Schroeder, Andrew Selle, Joseph Teran, and Alexey Stomakhin. The affine particle-in-cell method. *ACM Transactions on Graphics (TOG)*, 34(4):1–10, 2015. 3, 12
- [22] Chenfanfu Jiang, Craig Schroeder, Joseph Teran, Alexey Stomakhin, and Andrew Selle. The material point method for simulating continuum materials. In *ACM SIGGRAPH 2016 Courses*, New York, NY, USA, 2016. Association for Computing Machinery. 2, 3, 12
- [23] Chenfanfu Jiang, Theodore Gast, and Joseph Teran. Anisotropic elastoplasticity for cloth, knit and hair frictional contact. *ACM Transactions on Graphics (TOG)*, 36(4):1–14, 2017. 1, 2
- [24] Yingwenqi Jiang, Jiadong Tu, Yuan Liu, Xifeng Gao, Xiaoxiao Long, Wenping Wang, and Yuexin Ma. Gaussian-shader: 3d gaussian splatting with shading functions for reflective surfaces. In *Proceedings of the IEEE/CVF Conference on Computer Vision and Pattern Recognition*, pages 5322–5332, 2024. 2

- [25] Bernhard Kerbl, Georgios Kopanas, Thomas Leimkuehler, and George Drettakis. 3d gaussian splatting for real-time radiance field rendering. *ACM Transactions on Graphics (TOG)*, 42(4):1–14, 2023. 1, 2, 3, 4, 12
- [26] Gergely Klár, Theodore Gast, Andre Pradhana, Chuyuan Fu, Craig Schroeder, Chenfanfu Jiang, and Joseph Teran. Drucker-prager elastoplasticity for sand animation. *ACM Transactions on Graphics (TOG)*, 35(4):1–12, 2016. 3, 12
- [27] Xuan Li, Yi-Ling Qiao, Peter Yichen Chen, Krishna Murthy Jatavallabhula, Ming Lin, Chenfanfu Jiang, and Chuang Gan. PAC-neRF: Physics augmented continuum neural radiance fields for geometry-agnostic system identification. In *The Eleventh International Conference on Learning Representations*, 2023. 1, 2, 7
- [28] Yuchen Lin, Chenguo Lin, Jianjin Xu, and Yadong MU. OmniphysGS: 3d constitutive gaussians for general physics-based dynamics generation. In *The Thirteenth International Conference on Learning Representations*, 2025. 2
- [29] Fangfu Liu, Chubin Zhang, Yu Zheng, and Yueqi Duan. Semantic ray: Learning a generalizable semantic field with cross-reprojection attention. In *Proceedings of the IEEE/CVF Conference on Computer Vision and Pattern Recognition*, pages 17386–17396, 2023. 2
- [30] Shaohui Liu, Yinda Zhang, Songyou Peng, Boxin Shi, Marc Pollefeys, and Zhaopeng Cui. Dist: Rendering deep implicit signed distance function with differentiable sphere tracing. In *Proceedings of the IEEE/CVF conference on computer vision and pattern recognition*, pages 2019–2028, 2020. 2
- [31] Yuan Liu, Sida Peng, Lingjie Liu, Qianqian Wang, Peng Wang, Christian Theobalt, Xiaowei Zhou, and Wenping Wang. Neural rays for occlusion-aware image-based rendering. In *Proceedings of the IEEE/CVF Conference on Computer Vision and Pattern Recognition*, pages 7824–7833, 2022. 2
- [32] Aoran Lv, Yuanpeng Zhu, and Chuhua Xian. Efficient cloth simulation based on the material point method. *Computer Animation and Virtual Worlds*, 33(3-4):e2073, 2022. 2
- [33] Miles Macklin, Matthias Müller, and Nuttapong Chentanez. Xpbd: position-based simulation of compliant constrained dynamics. In *Proceedings of the 9th International Conference on Motion in Games*, pages 49–54, 2016. 1, 2
- [34] Ben Mildenhall, Pratul P Srinivasan, Matthew Tancik, Jonathan T Barron, Ravi Ramamoorthi, and Ren Ng. Nerf: Representing scenes as neural radiance fields for view synthesis. In *European Conference on Computer Vision*, pages 405–421. Springer, 2020. 1, 2, 5
- [35] Ashkan Mirzaei, Tristan Aumentado-Armstrong, Konstantinos G Derpanis, Jonathan Kelly, Marcus A Brubaker, Igor Gilitschenski, and Alex Levinstein. Spin-nerf: Multiview segmentation and perceptual inpainting with neural radiance fields. In *Proceedings of the IEEE/CVF Conference on Computer Vision and Pattern Recognition*, pages 20669–20679, 2023. 2
- [36] Matthias Müller, Bruno Heidelberger, Marcus Hennix, and John Ratcliff. Position based dynamics. *Journal of Visual Communication and Image Representation*, 18(2):109–118, 2007. 1, 2
- [37] Thomas Müller, Alex Evans, Christoph Schied, and Alexander Keller. Instant neural graphics primitives with a multiresolution hash encoding. *ACM transactions on graphics (TOG)*, 41(4):1–15, 2022. 2
- [38] Keunhong Park, Utkarsh Sinha, Jonathan T Barron, Sofien Bouaziz, Dan B Goldman, Steven M Seitz, and Ricardo Martin-Brualla. Nerfies: Deformable neural radiance fields. In *Proceedings of the IEEE/CVF international conference on computer vision*, pages 5865–5874, 2021. 2
- [39] Albert Pumarola, Enric Corona, Gerard Pons-Moll, and Francesc Moreno-Noguer. D-nerf: Neural radiance fields for dynamic scenes. In *Proceedings of the IEEE/CVF conference on computer vision and pattern recognition*, pages 10318–10327, 2021. 2
- [40] Maxime Raafat. BlenderNeRF, 2024. 5, 6
- [41] Daniel Ram, Theodore Gast, Chenfanfu Jiang, Craig Schroeder, Alexey Stomakhin, Joseph Teran, and Pirouz Kavehpour. A material point method for viscoelastic fluids, foams and sponges. In *Proceedings of the 14th ACM SIGGRAPH/Eurographics Symposium on Computer Animation*, pages 157–163, 2015. 3
- [42] Danila Rukhovich, Anna Vorontsova, and Anton Konushin. Fcaf3d: Fully convolutional anchor-free 3d object detection. In *European Conference on Computer Vision*, pages 477–493. Springer, 2022. 1
- [43] Tom FH Runia, Kirill Gavriluk, Cees GM Snoek, and Arnold WM Smeulders. Cloth in the wind: A case study of physical measurement through simulation. In *Proceedings of the IEEE/CVF conference on computer vision and pattern recognition*, pages 10498–10507, 2020. 1
- [44] Johannes L Schonberger and Jan-Michael Frahm. Structure-from-motion revisited. In *Proceedings of the IEEE conference on computer vision and pattern recognition*, pages 4104–4113, 2016. 5
- [45] Johannes L Schönberger, Enliang Zheng, Jan-Michael Frahm, and Marc Pollefeys. Pixelwise view selection for unstructured multi-view stereo. In *European conference on computer vision*, pages 501–518. Springer, 2016. 5
- [46] Yidi Shao, Mu Huang, Chen Change Loy, and Bo Dai. Gaussim: Foreseeing reality by gaussian simulator for elastic objects. In *Proceedings of the IEEE/CVF International Conference on Computer Vision (ICCV)*, pages 7841–7850, 2025. 2
- [47] Jin-Chuan Shi, Miao Wang, Hao-Bin Duan, and Shao-Hua Guan. Language embedded 3d gaussians for open-vocabulary scene understanding. In *Proceedings of the IEEE/CVF Conference on Computer Vision and Pattern Recognition*, pages 5333–5343, 2024. 2
- [48] Yawar Siddiqui, Antonio Alliegro, Alexey Artemov, Tatiana Tommasi, Daniele Sirigatti, Vladislav Rosov, Angela Dai, and Matthias Nießner. Meshgpt: Generating triangle meshes with decoder-only transformers. In *Proceedings of the IEEE/CVF conference on computer vision and pattern recognition*, pages 19615–19625, 2024. 2
- [49] Alexey Stomakhin, Craig Schroeder, Lawrence Chai, Joseph Teran, and Andrew Selle. A material point method for snow simulation. *ACM Transactions on Graphics (TOG)*, 32(4):1–10, 2013. 2, 3

- [50] Deborah Sulsky, Shi-Jian Zhou, and Howard L. Schreyer. Application of a particle-in-cell method to solid mechanics. *Computer physics communications*, 87(1-2):236–252, 1995. [1](#), [2](#)
- [51] Zeng Tao, Zheng Ding, Zeyuan Chen, Xiang Zhang, Leizhi Li, and Zhuowen Tu. C<sup>3</sup>editor: Achieving controllable consistency in 2d model for 3d editing. In *ICCV 2025 Workshop on Wild 3D: 3D Modeling, Reconstruction, and Generation in the Wild*, 2025. [2](#)
- [52] Thomas Unterthiner, Sjoerd Van Steenkiste, Karol Kurach, Raphael Marinier, Marcin Michalski, and Sylvain Gelly. Towards accurate generative models of video: A new metric & challenges. *arXiv preprint arXiv:1812.01717*, 2018. [7](#)
- [53] Nanyang Wang, Yinda Zhang, Zhuwen Li, Yanwei Fu, Wei Liu, and Yu-Gang Jiang. Pixel2mesh: Generating 3d mesh models from single rgb images. In *Proceedings of the European conference on computer vision (ECCV)*, pages 52–67, 2018. [2](#)
- [54] Tianyi Xie, Zeshun Zong, Yuxing Qiu, Xuan Li, Yutao Feng, Yin Yang, and Chenfanfu Jiang. Physgaussian: Physics-integrated 3d gaussians for generative dynamics. In *Proceedings of the IEEE/CVF Conference on Computer Vision and Pattern Recognition*, pages 4389–4398, 2024. [1](#), [2](#), [3](#), [4](#), [5](#), [7](#), [12](#)
- [55] Haiyang Xu, Yu Lei, Zeyuan Chen, Xiang Zhang, Yue Zhao, Yilin Wang, and Zhuowen Tu. Bayesian diffusion models for 3d shape reconstruction. In *Proceedings of the IEEE/CVF Conference on Computer Vision and Pattern Recognition*, pages 10628–10638, 2024. [2](#)
- [56] Qiangeng Xu, Zexiang Xu, Julien Philip, Sai Bi, Zhixin Shu, Kalyan Sunkavalli, and Ulrich Neumann. Pointnerf: Point-based neural radiance fields. In *Proceedings of the IEEE/CVF conference on computer vision and pattern recognition*, pages 5438–5448, 2022. [2](#)
- [57] Tianhan Xu and Tatsuya Harada. Deforming radiance fields with cages. In *European Conference on Computer Vision*, pages 159–175. Springer, 2022. [1](#), [2](#), [7](#)
- [58] Hongru Yan, Yu Zheng, and Yueqi Duan. Gaussian-det: Learning closed-surface gaussians for 3d object detection. In *The Thirteenth International Conference on Learning Representations*, 2025. [2](#)
- [59] Guandao Yang, Xun Huang, Zekun Hao, Ming-Yu Liu, Serge Belongie, and Bharath Hariharan. Pointflow: 3d point cloud generation with continuous normalizing flows. In *Proceedings of the IEEE/CVF international conference on computer vision*, pages 4541–4550, 2019. [2](#)
- [60] Yu-Jie Yuan, Yang-Tian Sun, Yu-Kun Lai, Yuewen Ma, Rongfei Jia, and Lin Gao. Nerf-editing: geometry editing of neural radiance fields. In *Proceedings of the IEEE/CVF conference on computer vision and pattern recognition*, pages 18353–18364, 2022. [1](#), [2](#), [7](#)
- [61] Yonghao Yue, Breannan Smith, Christopher Batty, Changxi Zheng, and Eitan Grinspun. Continuum foam: A material point method for shear-dependent flows. *ACM Transactions on Graphics (TOG)*, 34(5):1–20, 2015. [3](#)
- [62] Tianyuan Zhang, Hong-Xing Yu, Rundi Wu, Brandon Y Feng, Changxi Zheng, Noah Snively, Jiajun Wu, and William T Freeman. Physdreamer: Physics-based interaction with 3d objects via video generation. In *European Conference on Computer Vision*, pages 388–406. Springer, 2024. [5](#)
- [63] Xiang Zhang, Zeyuan Chen, Fangyin Wei, and Zhuowen Tu. Uni-3d: A universal model for panoptic 3d scene reconstruction. In *Proceedings of the IEEE/CVF International Conference on Computer Vision*, pages 9256–9266, 2023. [2](#)
- [64] Xiang Zhang, Yawar Siddiqui, Armen Avetisyan, Chris Xie, Jakob Engel, and Henry Howard-Jenkins. Vertexregen: Mesh generation with continuous level of detail. In *Proceedings of the IEEE/CVF International Conference on Computer Vision*, pages 12570–12580, 2025. [2](#)
- [65] Qingcheng Zhao, Xiang Zhang, Haiyang Xu, Zeyuan Chen, Jianwen Xie, Yuan Gao, and Zhuowen Tu. Depr: Depth guided single-view scene reconstruction with instance-level diffusion. In *Proceedings of the IEEE/CVF International Conference on Computer Vision*, pages 5722–5733, 2025. [2](#)
- [66] Yu Zheng, Yueqi Duan, Kangfu Zheng, Hongru Yan, Jiwen Lu, and Jie Zhou. Oponerf: One-point-one nerf for robust neural rendering. *arXiv preprint arXiv:2409.20043*, 2024. [2](#)
- [67] Licheng Zhong, Hong-Xing Yu, Jiajun Wu, and Yunzhu Li. Reconstruction and simulation of elastic objects with spring-mass 3d gaussians. In *European Conference on Computer Vision*, pages 407–423. Springer, 2024. [1](#), [2](#), [7](#)
- [68] Zeshun Zong, Xuan Li, Minchen Li, Maurizio M Chiaramonte, Wojciech Matusik, Eitan Grinspun, Kevin Carlberg, Chenfanfu Jiang, and Peter Yichen Chen. Neural stress fields for reduced-order elastoplasticity and fracture. In *SIGGRAPH Asia 2023 Conference Papers*, pages 1–11, 2023. [5](#), [12](#)

## A. Appendix

### A.1. MPM Algorithm

MPM simulates dynamic movements via discretizing a continuous body into particles and then updating their properties (including positions, velocities, etc.). We summarize the MPM algorithm as follows:

1. **Transfer Particles to Grid.** The mass and momentum from particles are transformed to grid nodes as

$$\begin{aligned} m_i^n &= \sum_p w_{ip}^n m_p, \\ m_i^n \mathbf{v}_i^n &= \sum_p w_{ip}^n m_p (\mathbf{v}_p^n + \mathbf{C}_p^n (\mathbf{x}_i - \mathbf{x}_p^n)), \end{aligned} \quad (\text{A.1})$$

where  $\mathbf{C}_p^n$  refers to affine momentum [21] on particle  $p$ .

2. **Grid Update.** Update grid velocities based on forces at the next timestep by

$$\frac{m_i}{\Delta t} (\mathbf{v}_i^{n+1} - \mathbf{v}_i^n) = - \sum_p \tau_p^n \nabla w_{ip}^n V_p^0 + \mathbf{f}_i^{ext}, \quad (\text{A.2})$$

3. **Transfer Grid to Particles.** Transfer velocities back to particles and update particle states.

$$\begin{aligned} \mathbf{v}_p^{n+1} &= \sum_i \mathbf{v}_i^{n+1} w_{ip}^n, \\ \mathbf{x}_p^{n+1} &= \mathbf{x}_p^n + \Delta t \mathbf{v}_p^{n+1}, \\ \mathbf{C}_p^{n+1} &= \frac{12}{\Delta x^2 (b+1)} \sum_i w_{ip}^n \mathbf{v}_i^{n+1} (\mathbf{x}_i^n - \mathbf{x}_p^n)^T, \\ \nabla \mathbf{v}_p^{n+1} &= \sum_i \mathbf{v}_i^{n+1} \nabla w_{ip}^n, \\ \mathbf{F}_p^{E,n+1} &= \mathcal{Z}((\mathbf{I} + \nabla \mathbf{v}_p^{n+1}) \mathbf{F}_p^{E,n}), \\ \tau_p^{n+1} &= \tau(\mathbf{F}_p^{E,n+1}). \end{aligned} \quad (\text{A.3})$$

Here  $b$  is the B-spline degree, and  $\Delta x$  is the Eulerian grid spacing. The deformation gradient  $\mathbf{F}_p = \mathbf{F}_p^E \mathbf{F}_p^P$  is decomposed into elastic part  $\mathbf{F}_p^E$  and plastic part  $\mathbf{F}_p^P$ . Detailed computation of the return map  $\mathcal{Z}$  and the Kirchhoff stress  $\tau$  is listed in Sec. A.2. Please refer to [22, 68] for more details.

### A.2. Details on Elastic and Plastic Models

In this section, we elaborate on the elastic and plastic constitutive models used in Gaussian Swaying, as listed in Tab. A.1. We adopt the models from [68].

#### A.2.1. Fixed Corotated Elasticity

The Kirchhoff stress  $\tau$  is defined as

$$\tau_p = 2\mu(\mathbf{F}_p^E - \mathbf{R}_p) \mathbf{F}_p^{E^T} + \lambda(J_p - 1)J_p, \quad (\text{A.4})$$

where  $\mathbf{R}_p = \mathbf{U}_p \mathbf{V}_p^T$  denotes local rotation and  $\mathbf{F}_p^E = \mathbf{U}_p \Sigma_p \mathbf{V}_p^T$  is the singular value decomposition of elastic deformation gradient.  $J_p$  is the determinant of  $\mathbf{F}_p^E$  [21].

#### A.2.2. Drucker-Prager Plasticity

Drucker-Prager plasticity is used for simulation of sand [26].

We set friction angle as  $\phi_f$  and  $\alpha = \sqrt{\frac{2}{3}} \frac{2 \sin \phi_f}{3 - \sin \phi_f}$ . We set  $\phi_f = 30^\circ$  in the experiment. Then we calculate intermediary variants:

$$\hat{\epsilon}_p = \epsilon_p - \frac{\text{tr}(\epsilon_p)}{d} \mathbf{I}, \quad \delta\gamma = \|\hat{\epsilon}_p\|_F + \alpha \frac{(d\lambda + 2\mu)\text{tr}(\epsilon_p)}{2\mu}, \quad (\text{A.5})$$

where  $\mathbf{F}_p^E = \mathbf{U}_p \Sigma_p \mathbf{V}_p^T$  and  $\epsilon_p = \log(\Sigma_p)$ .  $d$  is the dimension and  $\hat{\epsilon}_p$  is the plastic deformation amount.

The detailed calculation of return mapping  $\mathcal{Z}$  is given as

$$\mathbf{F}_p^E = \mathbf{U}_p \mathcal{Z}(\Sigma_p) \mathbf{V}_p^T, \quad (\text{A.6})$$

Here, if  $\text{tr}(\epsilon_p) > 0$ , then  $\mathcal{Z}(\Sigma_p) = 1$ .  $\mathcal{Z}(\Sigma_p) = \Sigma_p$  if  $\hat{\epsilon}_p \leq 0$  and  $\text{tr}(\epsilon_p) \leq 0$ . For other conditions,  $\mathcal{Z}$  is calculated as  $\exp\left(\epsilon_p - \delta\gamma_p \frac{\hat{\epsilon}_p}{\|\hat{\epsilon}_p\|}\right)$ .

### A.3. More Details on Parameters

We further provide detailed parameter settings, including Young's modulus  $E$ , Poisson's ratio  $\nu$ , mass density  $\rho$ , aerodynamic force coefficients  $\mathbf{C}_D$ ,  $\mathbf{C}_F$ ,  $\mathbf{C}_L$ , flow intensity and constitutive model of material in Tab. A.1. The constitutive model is defined the same with [54]. If the flow intensity changes during the simulation, it will be denoted by two values in the table (*Cloth* and *Vase* in Tab. A.1).

By default, we add three-dimension Gaussian noise with mean value 0 and standard deviation 0.3 to the wind speed to best approximate the behavior of the natural wind. The biggest component of the wind speed (e.g. 1.7 in *Leaves* in Tab. A.1) also serves the mean value of a sine function. The amplitude of the sine function is set to half of this component's value to simulate the swaying effect. In the flag simulation dataset, gravity is set as  $9.8m/s^2$ .

We train 3D Gaussians using the official implementation of [25] with proposed training losses. In Tab. A.2, we show-case ablation studies on Gaussian size, where  $b = 0.008$  is optimal for our setting. The total iterations are 60,000. In the simulation, Gaussians are filtered by an opacity threshold of 0.1 (In *Sand* we set it as 0.02). The frame number is 250, with each frame generated every 0.04s. The frame rate for the video is 25 for all experiments.

### A.4. More Results

We visualize qualitative comparisons with PhysGaussian in Fig. A.1. As shown, PhysGaussian fails to capture surface-level interaction (e.g., unrealistic leaf orientations in *Ficus* and *Leaves*, sand stretching rightward without scattering in *Sand*).

*Vase*, *Telephone* and *Alocasia* are real-world datasets to validate the application of Gaussian Swaying. In *Telephone*



Table A.1. **Parameter Settings.** We list the parameter settings on scenes in Gaussian Swaying.

Scene	Material				Aerodynamics			
	Constitutive Model	$E$	$\nu$	$\rho$	$C_D$	$C_F$	$C_L$	Flow Intensity
<i>Ficus</i> (Truck)	Fixed Corotated	2e6	0.4	300	0.5	0.4	0.01	(1.7, 0, 0)
<i>Leaves</i>	Fixed Corotated	1e4	0.4	15	0.5	0.4	0.01	(1.7, 0, 0)
<i>Sand</i>	Drucker-Prager	5e5	0.3	200	0.4	0.3	0.01	(10, 0, 0)
<i>Telephone</i>	Fixed Corotated	5e5	0.4	200	0.5	0.4	0.01	(-1, 0, 1)
<i>Alocasia</i>	Fixed Corotated	2e6	0.4	300	0.5	0.4	0.01	(0, -0.2, 0)
<i>Vase</i>	Fixed Corotated	1e4	0.3	20	0.4	0.3	0.005	(0, 0, -1.5), (0, 0, 1.5)
<i>Flag</i> (Pattern-1)	Fixed Corotated	5e3	0.3	50	-	-	-	(0, 0, 0)
<i>Flag</i> (Pattern-2)	Fixed Corotated	3e3	0.3	30	0.1	0.3	0.005	(2.5, 0.5, 0)
<i>Flag</i> (Pattern-3)	Fixed Corotated	3e3	0.3	20	0.1	0.3	0.005	(2, 0, 0)

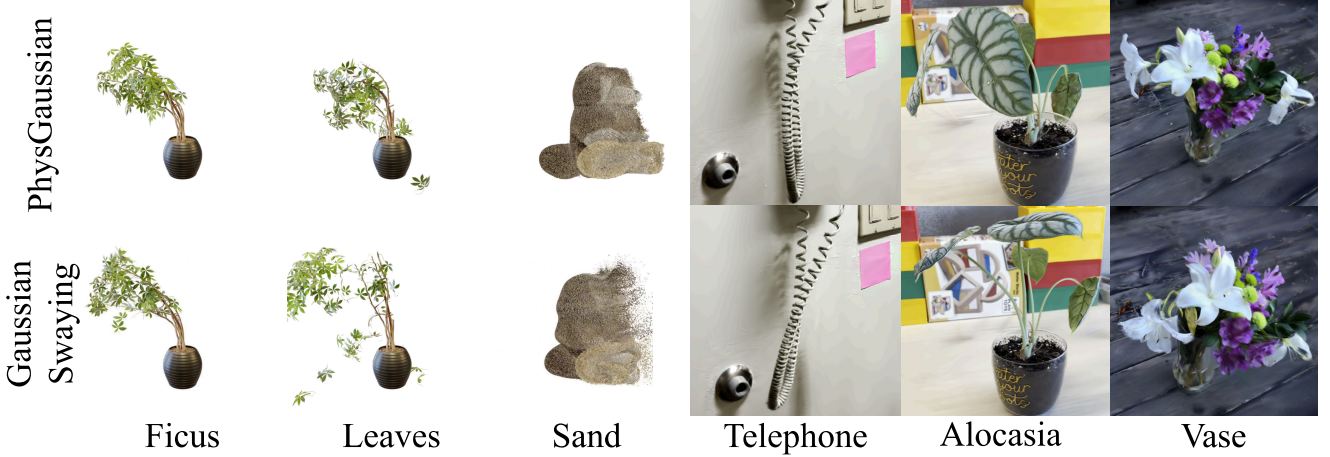


Figure A.1. Qualitative comparisons between PhysGaussian (*Upper Row*) and Gaussian Swaying (*Lower Row*).

Table A.2. **Ablation studies on Gaussian size.**

Param $b$	0.001	0.005	0.008	0.01	0.05	0.1
FVD ↓	362.77	248.66	<b>219.94</b>	432.88	796.01	910.24

and *Alocasia*, objects are applied with a gentle leftward incident flow. For comparisons, PhysGaussian unnaturally overstretches alocasia and telephone line, while ours accurately models leaf orientation and telephone line floating in the wind.

### A.5. Object Editing

To further demonstrate the flexibility and versatility of Gaussian Swaying, we explore its capability for real-time scene editing, including adjustments to material properties, colors, and interaction parameters. In Fig. A.2, the *Upper Row* is *Sand* while the *Lower Row* is edited to *Foam* with white color. Foam generally is stickier than sand, which aligns with the generated results by Gaussian Swaying.



Figure A.2. **Object Editing.** Gaussian Swaying is capable of realistic material and color editing to facilitate versatile applications. The top sand bear is edited to white foam at the bottom.

### A.6. Video Results

We provide video results in the supplementary materials. For example, detailed surface-level interactions between objects and wind can be best reflected in ‘Ficus.mp4’ and ‘Leaves.mp4’. In ‘Pattern3.mp4’, surface ripples can be

observed, which creates realistic visual effects. The reference videos of flag simulation are prefixed by “Reference-”. Compared with ‘Sand.mp4’, in ‘Sand\_All\_Gaussians.mp4’ the solid object is moving directly without surface deformation, which demonstrated the necessity of surface modeling.